



Experimental evidence for silica-enriched Earth's lower mantle with ferrous iron dominant bridgmanite

Izumi Mashino^{a,b,1}, Motohiko Murakami^{a,b}, Nobuyoshi Miyajima^c, and Sylvain Petitgirard^c

^aDepartment of Earth and Planetary Materials Science, Graduate School of Science, Tohoku University, Sendai, 980-8578 Miyagi, Japan; ^bDepartment of Earth Sciences, ETH Zürich, 8092 Zürich, Switzerland; and ^cBayerisches Geoinstitut, University of Bayreuth, 95440 Bayreuth, Germany

Edited by Ho-kwang Mao, Center for High Pressure Science and Technology Advanced Research, Shanghai, China, and approved September 22, 2020 (received for review October 2, 2019)

Determination of the chemical composition of the Earth's mantle is of prime importance to understand the evolution, dynamics, and origin of the Earth. However, there is a lack of experimental data on sound velocity of iron-bearing Bridgmanite (Brd) under relevant high-pressure conditions of the whole mantle, which prevents constraints on the mineralogical model of the lower mantle. To uncover these issues, we have conducted sound-velocity measurement of iron-bearing Brd in a diamond-anvil cell (DAC) up to 124 GPa using Brillouin scattering spectroscopy. Here we show that the sound velocities of iron-bearing Brd throughout the whole pressure range of lower mantle exhibit an apparent linear reduction with the iron content. Our data fit remarkably with the seismic structure throughout the lower mantle with Fe²⁺-enriched Brd, indicating that the greater part of the lower mantle could be occupied by Fe²⁺-enriched Brd. Our lower-mantle model shows a distinctive Si-enriched composition with Mg/Si of 1.14 relative to the upper mantle (Mg/Si = 1.25), which implies that the mantle convection has been inefficient enough to chemically homogenize the Earth's whole mantle.

sound velocity | high pressure | mineralogical model of the lower mantle | iron spin-state change of bridgmanite

Identification of the chemical compositions of the Earth's upper and lower mantle provides critical implications for the geochemical, geophysical, seismological, and cosmochemical models of the Earth. However, this issue has yet to be resolved. While the Mg/Si ratio of the upper mantle has been believed to be approximately ~1.25 based on geochemical and petrological observations (1–3), the Mg/Si ratio of the lower mantle still remains unknown because of a lack of direct observations and conclusive experimental results.

The dominant minerals in the lower mantle are thought to be Fe-bearing MgSiO₃ bridgmanite (Brd) and (Mg, Fe)O ferropericlase (Fp). This mineralogical model can be primarily constrained by measuring experimentally the sound velocities of those minerals together with the mantle geotherm and by comparing with the seismological data. Although the sound-velocity measurements of those mineral phases have recently been achieved under high-pressure and -temperature conditions relevant to the deep lower mantle (4, 5), the effect of iron in Brd on the sound velocities under such conditions has not experimentally been explored for the whole mantle. Previous studies showed that the spin transition of iron in Fp notably affects its elastic properties (5–12). Previous computational studies showed that the spin transition of iron in Fp leads to anticorrelation between V_{ϕ} and V_S in the mid-lower mantle, although the spin transition in Fp might not generate an obvious signature in one-dimension velocity profiles (11, 12). In contrast, the presence and effect of the spin transition in Fe-Brd still remains unclear compared to that of Fp. Under the assumption that the lower mantle has a pyrolitic bulk chemical composition, Fe-Brd is widely thought to occupy around 80 vol % of the lower mantle; therefore, its properties should have a significant effect on the mineralogical model of the lower mantle. It is suggested that the

spin change in Fe-Brd might occur up to ~60 GPa based on previous extensive spectroscopic works and computational studies (13–17). However, the existence and effect of the spin change have not been clarified because of its complicating factors such as the valence states of iron (Fe²⁺, Fe³⁺) and their site occupancies. Recently, Fu et al. (18) conducted the sound-velocity measurements on Brd up to 70 GPa to explore the exact pressure range of spin transition of Fe³⁺ in Brd, and suggested that spin transition of Fe³⁺ occurs from 42.6 to 58 GPa by the trend change of the velocity. In contrast to phases in the upper mantle, the Fe³⁺/ΣFe ratio in the lower mantle has been believed to be relatively high because the amount of ferric iron in Fe-Brd possibly ranges from ~20% to more than ~60% with increasing Al content (19–21). A recent study suggested that the shallow lower mantle has a high Fe³⁺/ΣFe ratio with a decreasing Fe³⁺/ΣFe ratio from 0.66 to 0.33 with increasing pressure while the Fe²⁺/ΣFe ratio increases within the investigated pressure range up to ~40 GPa (22). However, their results have been criticized that careful sensitivity test between measured velocities and elastic constants and a covariance matrix analysis showed that their derived elastic constants and velocities have large uncertainties at lower-mantle pressures, which might invalidate their assertions related to the lower-mantle mineralogy (23). Furthermore, their results are only based on the limited experimental pressures up to ~40 GPa, out of the pressure range where the spin transition of iron in Brd is considered to occur (22, 24), and most of the lower part of the lower mantle has yet to be explored.

Significance

Iron-bearing bridgmanite is the most abundant mineral in the Earth's interior. We overcome the experimental challenge of measuring iron-bearing materials by using Brillouin scattering techniques optimized for extreme pressure conditions in combination of diamond-anvil cell. By using such techniques, results of acoustic wave velocities in the pressure range of the entire mantle are reported here. Based on our results, we show that the greater part of the lower mantle is Fe²⁺-rich because the gradient of our model gives excellent fit to that of Preliminary Reference Earth Model for almost all the pressure range of the lower mantle with an Fe³⁺/ΣFe of 0.2. Our lower-mantle model also shows a distinctive Si-enriched composition with Mg/Si of 1.14 relative to the upper mantle.

Author contributions: I.M. and M.M. designed research; I.M., M.M., N.M., and S.P. performed research; I.M. and N.M. analyzed data; and I.M., M.M., N.M., and S.P. wrote the paper.

The authors declare no competing interest.

This article is a PNAS Direct Submission.

Published under the PNAS license.

¹To whom correspondence may be addressed. Email: izumi.mashino@okayama-u.ac.jp.

This article contains supporting information online at <https://www.pnas.org/lookup/suppl/doi:10.1073/pnas.1917096117/-DCSupplemental>.

First published October 22, 2020.

The shear modulus is likely to be more sensitive to such changes in the structure than the bulk modulus according to previous X-ray diffraction (XRD) measurements (16, 25), therefore, it is important to measure the V_S of the Fe-bearing Brd under lower-mantle pressures to determine the effect of the spin state.

Here, we present the results of acoustic wave velocity measurements on Fe-Brd by Brillouin spectroscopy in the diamond-anvil cell (DAC) up to 124 GPa, which covers the whole lower-mantle pressure regime, to clarify the potential effect of the spin-state change of Fe^{2+} in Brd on the lower mantle.

Results

We conducted two separate series of in situ high-pressure Brillouin scattering measurements using DACs and obtained the acoustic velocities for two different Fe-Brd compositions with $(Mg_{0.93}Fe^{2+}_{0.07})(Fe^{3+}_{0.02}Si_{0.98})O_3$ (Brd01&03) and $(Mg_{0.86}Fe^{2+}_{0.15})(Fe^{3+}_{0.03}Si_{0.97})O_3$ (Brd02&04) from 25.9 to 124.4 GPa at ambient temperature condition. As shown in Fig. 1 A and B, we obtained sharp peaks from the shear acoustic mode (V_S) of Fe-Brd over the entire pressure range explored (see also *SI Appendix, Table S1*). We have also paid special attention to the characterization of recovered samples to carefully check if there are any changes in crystallinity and chemistry of the samples since they might significantly affect the elasticity data (see also *Materials & Methods*, and *SI Appendix, Supplementary Materials* in detail). Fig. 1 C–F show the typical selected area electron diffraction (SAED) patterns and bright-field transmission electron microscopy (TEM) images of the samples recovered from the high-pressure acoustic velocity measurements. From the bright-field TEM images (Fig. 1 C and D), we can easily recognize the well-sintered Fe-Brd grains having an ~ 100 – 500 -nm grain size with distinctive grain boundaries. The clear diffraction spots can be indexed to the crystal structure of Brd with an orthorhombic cell, indicating that the recovered Fe-Brd samples, synthesized under high pressures, have preserved high crystallinity. To characterize the valence state of the iron in Fe-Brd, we also determined the $Fe^{3+}/\Sigma Fe$ ratios of these samples by using electron energy-loss spectroscopy (EELS) and found values $0.17(\pm 0.05)$ and $0.21(\pm 0.05)$ for Brd01 and Brd02, respectively (Fig. 1G). The TEM analysis of the chemical composition mapping of the recovered samples using the high-angle annular dark-field (HAADF) and energy-dispersive X-ray (EDX) method did not show any significant spatial distribution in iron content across the sample (*SI Appendix, Fig. S1 and Materials and Methods*). The aggregate shear velocities as a function of pressure (Fig. 2) were fitted to third-order Eulerian finite-strain equations (26) to obtain the adiabatic shear modulus, G , and its pressure derivative, G' . For this regression, we adopted the zero-pressure volumes, isothermal bulk modulus, and pressure derivative of the bulk modulus ($K' = 4.0$) from recent high-pressure experiments (27, 28). We obtained best-fit values of $G_0 = 165.8$ (13) GPa and $G'_0 = 1.76$ (4) for Brd01&03 and $G_0 = 167.5$ (17) GPa with a $G'_0 = 1.78$ (6) GPa for Brd02&04 (*SI Appendix, Table S2*).

Discussion

The shear-wave velocity profiles of Brd as a function of Fe content are shown in *SI Appendix, Fig. S2*. The shear-wave velocities of Brd decrease with Fe content and can be reasonably fitted by a linear relationship. This relationship is consistent with previous predictions based on computational studies (30, 31).

Our results cover the entire pressure range of the lower mantle and allow us to put stronger constraints on the mineralogical model of the lower mantle taking the effect of iron content in Brd into account. In the modeling, we assume a simplified lower-mantle lithology with a two-phase mixture of $(Mg_{0.93}Fe^{2+}_{0.07})(Fe^{3+}_{0.02}Si_{0.98})O_3$ Brd measured in this study and $(Mg_{0.79}Fe_{0.21})O_3$ Fp from previous

experimental study (5). We adopted the representative iron partitioning relationship between Brd and Fp based on previous study (32). Since the effect of Al has also been reported to be negligibly small in previous studies (5, 33), the effect of Al content in Brd on the velocity was ignored. The trade-offs between Mg/Fe or Mg/Si and thermal parameters were discussed in previous studies (34, 35). We use thermal parameters of $MgSiO_3$ Brd obtained by previous studies (*SI Appendix, Table S3*). In general, the main uncertainties in the mineralogical modeling reflect the errors in the thermodynamic and thermoelastic parameters have been used. The effect of temperature on the shear modulus is most sensitive to η_{S0} , the shear-strain derivative of the Grüneisen parameter (34). In addition to η_{S0} , we consider the bulk modulus K_0 , shear modulus G_0 , and its pressure derivative G'_0 . The calculation of propagating uncertainties for all parameters simultaneously is difficult (36), so we consider the uncertainties of the model for each parameter individually. A variation of K_0 , G_0 , G'_0 , and η_{S0} , which covers nearly the entire range of reported values, changes the volumetric percentage of Brd in the lower mantle (X_{Brd}) by less than 3%. A variation of K'_0 , θ_0 , γ_0 , q_0 , which covers nearly the entire range of reported values, changes the X_{Brd} by less than $\sim 0.1\%$. Although the temperature effect of spin-state change on the elastic properties of Brd is not completely understood yet, previous studies suggested that the spin-transition zone widens and shifts toward higher pressure (~ 20 GPa) with increasing temperature (7, 9, 15). In order to evaluate the effect of temperature on the uncertainties of the mineralogical model of the lower mantle, we calculated the X_{Brd} when the spin-state change shifts to 20 GPa higher in pressure. The shift to higher pressure of 20 GPa changes the X_{Brd} by less than 1%, thus, the temperature-induced shift of spin transition does not change our final conclusion. Kuznetsov et al. (15), conducted in situ high-pressure and -temperature Mössbauer spectroscopic measurements up to 80 GPa and $\sim 2,000$ K. They show that the $\Sigma Fe^{2+}/Fe$ ratio in Fe-Brd itself does not change at high temperature. This means that we can assume that the $\Sigma Fe^{2+}/Fe$ ratio in Fe-Brd under the mantle geotherm condition is the same as that of ambient temperature. For our calculation, we used the lower-mantle geotherm for a whole-mantle convection model proposed by Katsura et al. (T-K) (37) because the 410-km discontinuity used as a fixed point is more appropriate and also it includes the latest experimental results for the thermal parameters of minerals. The temperature profile of the lower mantle does not display any thermal boundary layer between upper and lower mantle. In parallel, we also modeled the geotherm assuming the thermal boundary layer between upper and lower mantle by Anderson (O-A) (38) for a layered mantle convection model. The aggregate V_S values of the two-phase assemblage were obtained by the Voigt–Reuss–Hill averaging method (36). We compared the calculated V_S profiles with one-dimensional global seismic model of the Preliminary Reference Earth Model (PREM) (39). The latter is best fitted by a mixture of 88% Brd and 12% Fp by volume for the T-K geotherm (Fig. 3B), and 92% Brd and 8% Fp by volume for the O-A geotherm (Fig. 3C). Furthermore, we also found that the present V_S profile gave much better fitting with PREM than without considering the effect of possible spin-state change of iron in Brd. In Fe-Brd, some conflicting interpretations of the spin states of Fe^{2+} have so far been proposed including high-spin (HS) to intermediate-spin (IS) transition proposed by experimental studies (14, 15, 40), or low-to high-QS (iron Mössbauer quadrupole splitting) transition proposed by theoretical studies (16, 17). Although it has been suggested that IS state of Fe-Brd could be experimentally measurable (14), it is still unclear whether the spin transition really plays a dominant/detectable role on the elasticity. So far, it has been suggested that Fe^{3+} in the A site remains in the HS state and Fe^{3+} in the B site becomes the LS state up to 36 GPa, and the effect of spin transition on physical properties is small

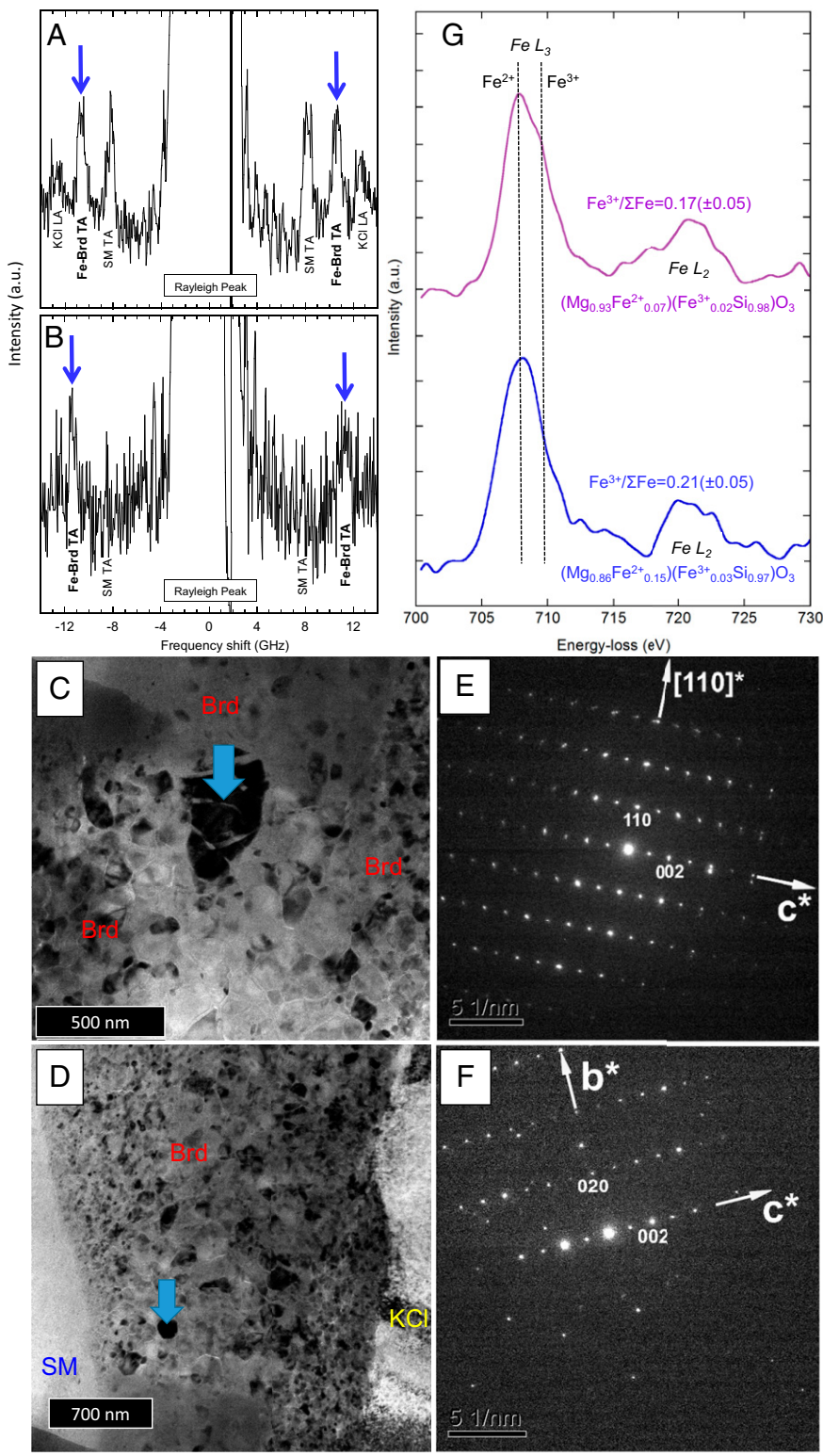


Fig. 1. Representative Brillouin spectra, SAED patterns, bright-field TEM images, and TEM-EELS spectra of Fe-Brd. (A and B) Brillouin spectra of Fe-Brd at 31.8 GPa (A) and 105.1 GPa (B). Fe-Brd, (Mg,Fe)SiO₃ bridgmanite; SM, starting material; TA, transverse acoustic modes of the Brillouin shift. (C–F) SAED patterns and bright-field TEM images of recovered samples. (E and F) The [110]* and [100] zone axis diffraction patterns of Brd crystals pointed at by blue arrows on the bright-field TEM images of c and d, respectively. (G) TEM-EELS spectra of Fe-Brd. The quantitative determination of the Fe³⁺/ΣFe ratio was based on the black dotted lines intensities at the Fe L_{2,3}-edge.

due to the limited amount of Fe³⁺ in the LS state (41–43). Recent experimental study suggested that the spin transition of Fe³⁺ also occurs to 60 GPa (18). Previous studies also suggested

that the boundary of the transition of Fe²⁺ from HS to IS not sharp. Kupenko et al. (44) shows that the HS/IS ratio gradually decreases with increasing pressure from 30 to 50 GPa. Although

Downloaded at Palestinian Territory, occupied on December 27, 2021

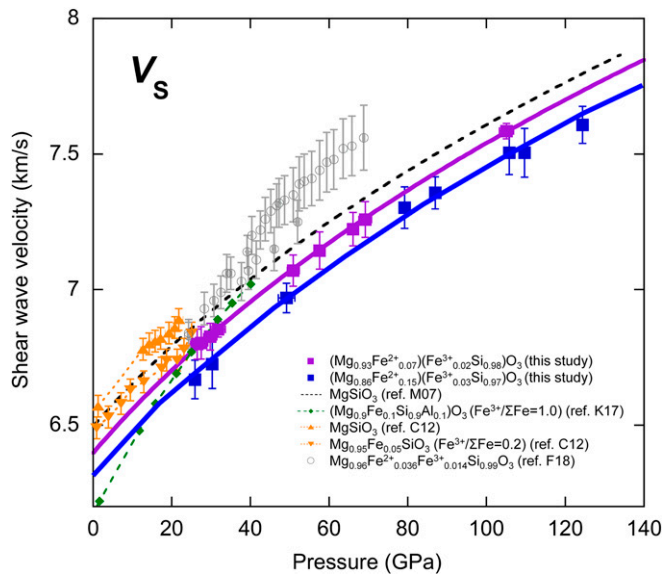


Fig. 2. Shear-wave velocity profiles of Brd as a function of pressure at 300 K. Blue and purple squares show the shear-wave velocities of $(\text{Mg}_{0.96}\text{Fe}^{2+}_{0.15})(\text{Fe}^{3+}_{0.03}\text{Si}_{0.97})\text{O}_3$ and $(\text{Mg}_{0.93}\text{Fe}^{2+}_{0.07})(\text{Fe}^{3+}_{0.02}\text{Si}_{0.98})\text{O}_3$ Brd, respectively. Third-order Eulerian finite strain fits are shown by solid lines. Black dotted lines show the shear-wave velocity profiles of MgSiO_3 from M07 (29) by Brillouin measurements. Orange upward- and downward-pointing triangles show the shear-wave velocity profiles of MgSiO_3 and $\text{Mg}_{0.95}\text{Fe}^{2+}_{0.04}\text{Fe}^{3+}_{0.01}\text{SiO}_3$ Brd from C12 (24) by ultrasonic measurements, green diamonds shows that of $(\text{Mg}_{0.9}\text{Fe}_{0.1}\text{Si}_{0.9}\text{Al}_{0.1})\text{O}_3$ Brd from K17 (22) by Brillouin scattering measurements, and gray circles shows that of $\text{Mg}_{0.96}\text{Fe}^{2+}_{0.036}\text{Fe}^{3+}_{0.014}\text{Si}_{0.99}\text{O}_3$ Brd from F18 (18) by Brillouin scattering measurements, respectively.

our purpose is not to determine the exact pressure range of the spin transition, we compare the lower-mantle model using the data only below 50 GPa and using all of the data we took because most of the spin-state changes of Fe generally occur around 50 GPa. As shown in Fig. 4, the V_S profile without considering the effect of the possible spin-state change (using the data only below 50 GPa) exhibited the systematic deviation from PREM at the base point around 50 GPa, and its deviation becomes up to $\sim 2\%$ at the bottom of the lower mantle. The inclination of the V_S profile has been changed by the spin-state change as shown in Fig. 4. Therefore, the V_S and G' are strongly affected by the spin-state change in Fe-Brd. While the effect of the iron spin-state change on the density has been thought to be a negligible effect on the X_{Brd} relative to the possible uncertainty of the seismic model (45), our results show that its effect with more than $\sim 2\%$ change in seismic velocity could be detectable by seismic observations. Although any possibility of hyperfine structure of Fe in Brd cannot be ruled out because we did not conduct direct measurements of spin state of iron, our experimental results thus strongly indicate that the spin-state change of iron in Brd is essentially required to reasonably explain the one-dimensional seismic velocity model. We also calculated the V_P profile using the bulk modulus (K) and density (ρ) [$V_P = \sqrt{((K + 4G/3)/\rho)}$, $V_S = \sqrt{(G/\rho)}$] determined from recent XRD data (46, 47) although V_S has higher sensitivity to composition (48, 49). We compared the calculated V_P profile with one-dimensional global seismic model of PREM. The latter is best fitted by a mixture of 93% Brd and 8% Fp by volume for the O-A shown in *SI Appendix, Fig. S3*. The X_{Brd} s in the V_S ($X_{\text{Brd}} = 0.92$) and V_P ($X_{\text{Brd}} = 0.93$) show good agreement with each other. This result also strengthens the robustness of our lower-mantle model obtained from V_S data.

As shown in Fig. 3, the gradient of P - V_S profile of our mineralogical model is also in good agreement with PREM. The $\text{Fe}^{3+}/\Sigma\text{Fe}$ ratio in Brd has been under debate so far, which is known as the paradox of the mantle redox (19, 21, 50). Very

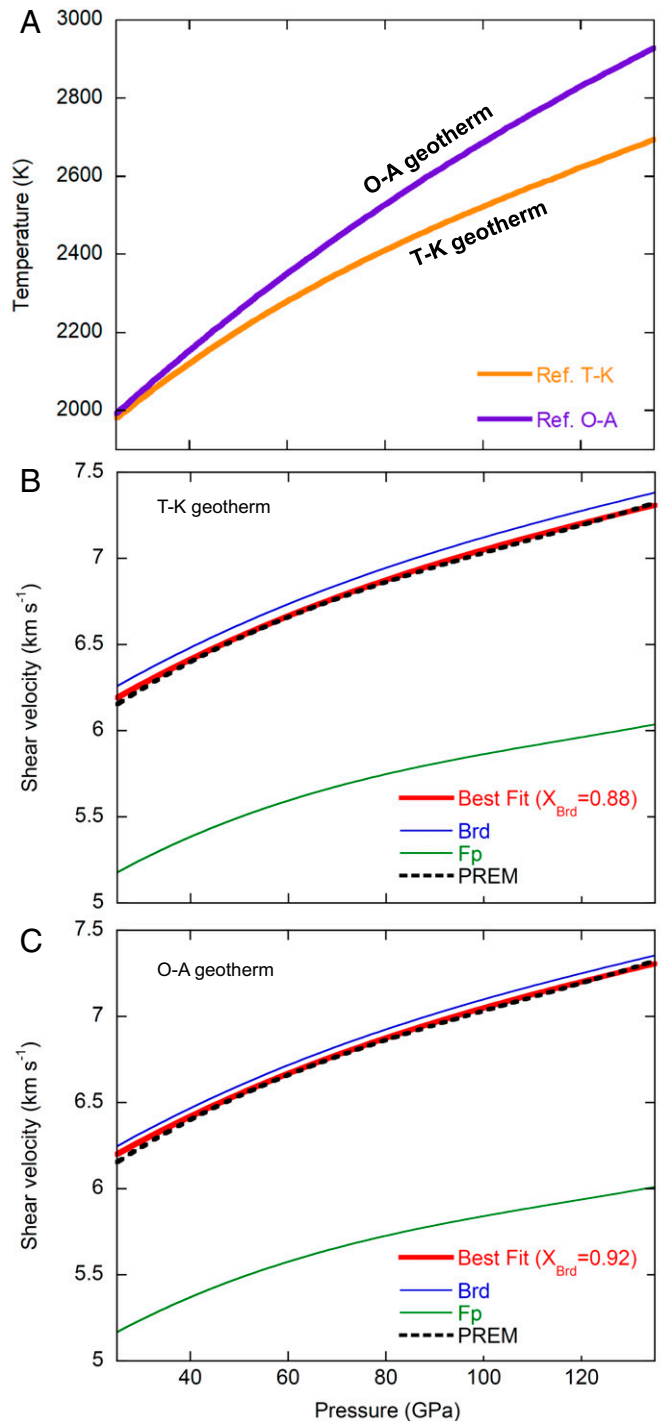


Fig. 3. Lower-mantle geotherms and calculated shear-wave velocity profiles. (A) Representative lower-mantle geotherms for T-K (37) and O-A (38). (B and C) Calculated shear-wave velocity profiles for T-K (37) (B) and O-A (38) (C). Calculated shear-wave velocity profiles of Fe-Brd (blue lines), Fp (green lines), and PREM (dashed black lines). The best-fit models to PREM are shown as red curves. The uncertainties fall in the line thicknesses, which derived from the uncertainties of the shear-strain derivative of the Grüneisen parameter η_{50} .

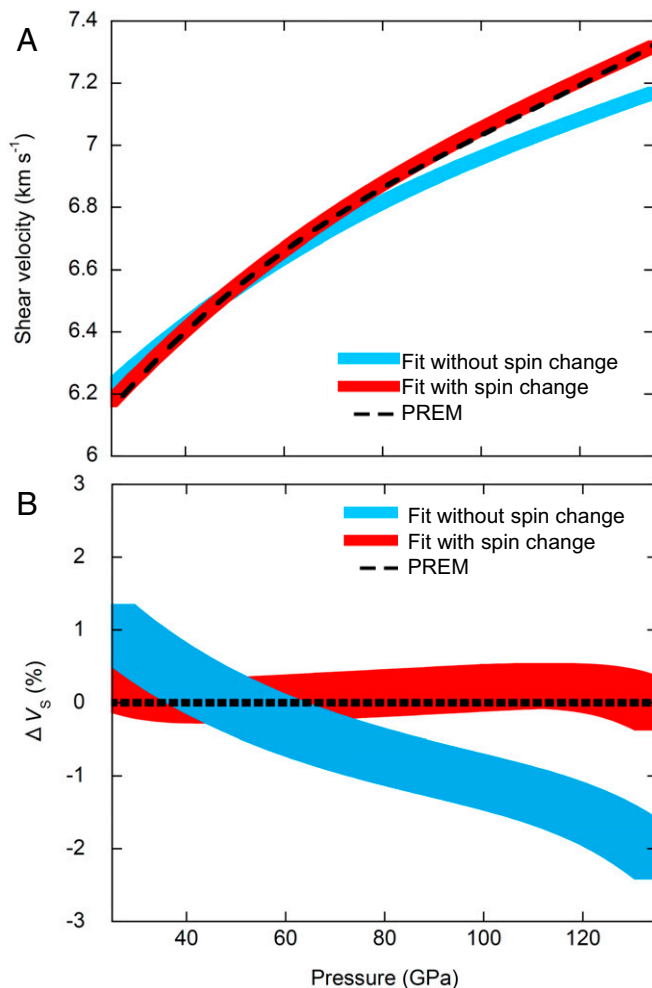


Fig. 4. Effect of the spin transition on the mineralogical model of the lower mantle. (A) Calculated V_s profile using the data without the effect of the spin-state change (Fit without spin change) with that of the entire pressure range including the effect of the spin-state change in Fe-Brd (Fit with spin change) in the case of the mixture of 92% Brd and 8% Fp by volume for O-A geotherm (38). Dashed black lines are PREM. (B) Relative deviations of the calculated V_s profile of Fit without spin change and Fit with spin change are shown as percentages taking PREM values as reference. The uncertainties fall in the line thicknesses, which derived from the uncertainties of the shear-strain derivative of the Grüneisen parameter η_{50} .

recently, Kurnosov et al. (22) showed that Brd in the uppermost lower mantle has a high $\text{Fe}^{3+}/\Sigma\text{Fe}$ ratio, whereas the $\text{Fe}^{3+}/\Sigma\text{Fe}$ ratio in Brd should decrease to ~ 0.33 for pressure above 50 GPa (1,200 km); however, the mineralogical model invoked cannot explain PREM below 1,200-km depth. This is because the gradient of P - V_s profile of Fe^{3+} -Brd is much steeper than those of PREM and Mg-Brd (Fig. 2). The gradient of our model gives excellent fit to that of PREM for almost all of the pressure range of the lower mantle, while its gradient and velocity are gentler and $\sim 0.4\%$ faster than those of PREM under ~ 40 GPa. Kurnosov et al. showed that their best-fitted model using the Fe^{3+} -Brd with an $\text{Fe}^{3+}/\Sigma\text{Fe}$ ratio of 0.66 at 30 GPa is 0.4% lower than PREM. The velocity difference between our model and PREM also corresponds reasonably well with the difference between the Kurnosov model and PREM. Thus, Brd in the shallow part of the lower mantle has a high Fe^{3+} content, while Brd in the middle and lower parts of the lower mantle becomes Fe^{2+} -rich, with an $\text{Fe}^{3+}/\Sigma\text{Fe}$ of 0.2 as proposed in our model. Our model is also compatible with the hypotheses for Fe^{2+} -enriched LLSVPs

(large low-shear-velocity provinces) (51). Therefore, our results also support that the greater part of the lower mantle is Fe^{2+} -rich. Such a high Fe^{2+} content in Brd would affect the mantle convection and also would be a key to understand the evolution of the Earth.

Furthermore, the Mg/Si ratio of the lower mantle can be calculated based on the amount of Fe-Brd and Fp in our mineralogical model of the lower mantle, 88% Brd and 12% Fp by volume for the T-K geotherm as well as 92% Brd and 8% Fp by volume for the O-A geotherm. Many previous studies have so far considered that the mantle would be chemically homogeneous with a pyrolitic composition (22, 24, 52). Our mineralogical modeling shows that the lower mantle is expected to be $\sim 20\%$ richer in silicon on an atomic basis ($\text{Mg/Si} = \sim 1.1$) than the upper mantle ($\text{Mg/Si} = \sim 1.25$) as shown in *SI Appendix, Fig. S4*. One of the major reasons that supports a pyrolitic lower mantle is that previous seismic tomography studies provided us the seismic views that some of the subducting slabs are penetrating through the boundary between the upper and lower mantle, which should enhance the chemical homogenization of the mantle (53, 54). However, seismic tomography images have also put into evidence that the stagnation of the slabs in the mantle transition zone or at $\sim 1,000$ -km depth (55) is possible. Such diversities in the subduction style of slabs thus do not necessarily imply that the whole-mantle convection model is predominant in the present day Earth. In fact, recent geodynamical simulation study reported that the mantle should be partially layered with a silica-enriched lower mantle ($\text{Mg/Si} = 1.18$) in order to explain seismic tomography images of stagnant slabs at $\sim 1,000$ km (56), which is compatible with our mineralogical modeling. It is also believed that the convection style of the mantle evolved with the Earth's history. Previous geodynamical calculations proposed that the convection style should change from two-layered to whole-mantle convections mainly because of the decrease of the Rayleigh number with time (57, 58). Although it is still unclear how long the layered mantle convection had played a dominant role in the mantle chemistry throughout the Earth's history if such evolving scenario were the case, our results strongly suggest that mantle mixing has not been efficient throughout the Earth's history to homogenize the whole-mantle composition, and the present Earth might be on a transitional stage from the layered mantle convection to whole-mantle convection judging from the varieties (*SI Appendix, Fig. S5*).

Finally, a recent advanced study of geoneutrinos (59) has evaluated various bulk silicate Earth composition models based on the observed geoantineutrinos rate. It was not until the recent long-term shutdown of Japanese nuclear reactors that this pioneering measurement was eventually achieved, which can provide much more reliable data with low backgrounds and improved sensitivity for the antineutrinos (59). The measurements show that the Earth's lower mantle should have silica-enriched composition relative to the upper mantle, which again support a Si-rich lower-mantle model with a Mg/Si of ~ 1.14 . The recalculated average whole-mantle composition was then found to have a Mg/Si ratio of ~ 1.2 based on the assumption that the upper-mantle and mantle-transition zone have a pyrolitic composition relative to CI chondrites ($\text{Mg/Si} = 1.0\sim 1.1$) (2, 60, 61). The future determination of the lower-mantle geotherm, and of the chemistry of upper-mantle and mantle-transition zone should be able to put much tighter constraints on the Earth's building materials issue.

Materials and Methods

Preparation of Starting Material. We used enstatite gels of Fe-MgSiO_3 contains 1.8 wt % and 3.3 wt % Fe as starting materials with $\text{Fe}^{3+}/\Sigma\text{Fe}$ ratio of 0.4. The gels were synthesized from tetraethyl orthosilicate ($\text{C}_2\text{H}_5\text{O}_4\text{Si}$), magnesium nitrate $\text{Mg}(\text{NO}_3)_2 \cdot 6\text{H}_2\text{O}$, and powdered ^{57}Fe metal (96.63%

enriched in ^{57}Fe) by a sol-gel method. The enstatite gels were placed in a platinum crucible and heated under reducing conditions using a H_2/CO_2 gas-flow furnace at 750 °C and subsequently quenched by immersing the base of the crucible in liquid nitrogen.

A symmetric-type DAC with a culet size of 130 and 150 μm was used to generate high pressure. Rhenium gaskets were preindented to $\sim 35\text{-}\mu\text{m}$ thickness before laser drilling or spark erosion of $\sim 40\text{-}\mu\text{m}$ -diameter holes. Sample pellets were loaded between two pieces of dry KCl with thicknesses of $\sim 5\text{ }\mu\text{m}$, which served as pressure-transmitting medium and thermal insulator from the diamonds. Pressure was determined using ruby fluorescence (62) by measuring several points adjacent to the measurement position. Fe-Brd phases were synthesized from the enstatite gels at 31.8 for run#Brd01, 49.2 GPa for run#Brd02, 26.5 GPa for run#Brd03, and 25.9 GPa for run#Brd04 using CO_2 lasers for 5 min on each of the upper and lower sides of the sample, respectively. Because iron diffuses easily by laser heating, we did not reheat the samples in order to avoid measuring Brds which have different iron concentrations at each pressure point.

Acoustic Wave Velocity Measurement by Brillouin Spectroscopy. In situ high-pressure Brillouin scattering measurements of acoustic wave velocities were carried out at room temperature in a symmetric DAC using the measurement systems at Tohoku University and ETH Zürich. A diode-pumped laser with a wavelength of 532 nm (Verdi V2, V6, Coherent) was used as a probe beam. The incident laser beam was focused to a spot size of $\sim 10\text{-}\mu\text{m}$ diameter on the sample. In all measurements, symmetric scattering geometry with an $\sim 50^\circ$ external scattering angle was used. For calibration of the scattering geometry in the present system, a borosilicate crown optical glass (BK7) with high purity, optical homogeneity, and high transmission in wide wavelength range (350–2,000 nm) was used as a standard material. For this purpose, a 50- μm -thick thin section of doubly polished BK7 under ambient conditions in a symmetric geometry was measured. From the Brillouin shifts from BK7, the external scattered angle was calibrated by comparing the results with literature data determined by ultrasonic interferometry.

The scattered light was collected and passed through a Sandercock-type six-pass Fabry–Perot interferometer and recorded with a multichannel analyzer (GHOST v.6.0.0, JRS Scientific Instruments). The scattered light comprises an elastically scattered component with frequency, ω , together with Brillouin-scattered components with a frequency shift, $\Delta\omega$, which results from interaction with thermally generated phonons in the sample. In a symmetric scattering geometry, the velocity V of an acoustic wave is calculated without knowledge of the sample refractive index from the relation

$$V_i = \frac{\Delta\omega_i \lambda}{2 \sin\left(\frac{\theta^*}{2}\right)}$$

where λ is the laser wavelength (532 nm) and θ^* is the external scattering angle, and i denotes one of the acoustic modes.

Brillouin spectra were collected at 17 pressures from 25.9 to 124.4 GPa in four separate experimental runs at ambient temperature. We conducted four independent series of Brillouin scattering measurements, from 26.5 to 105.1 GPa for $(\text{Mg}_{0.93}\text{Fe}^{2+}_{0.07})(\text{Fe}^{3+}_{0.02}\text{Si}_{0.98})\text{O}_3$ (Run#Brd01, Brd03) and from 25.9 to 124.4 GPa for $(\text{Mg}_{0.86}\text{Fe}^{2+}_{0.14})(\text{Fe}^{3+}_{0.03}\text{Si}_{0.97})\text{O}_3$ (Run#Brd02, Brd04). The cells were annealed in a vacuum oven at 200 °C for about 24–48 h to relax deviatoric stresses in the sample chamber at all data points (see also *SI Appendix, Supplementary Discussion*). The acquisition times for Brillouin scattering measurements were from 150 to 350 h, depending mainly on pressure. At each pressure, the individual raw Brillouin spectra were fitted with a Gaussian peak function and the peak positions were recorded. The average of the peak positions, including Stokes and anti-Stokes signals, of all spectra at a given pressure was used.

We also collected Brillouin spectra of Fe-Brd at several pressures in four directions in the scattering plane with a typical angular increment of 30° between data points randomly by rotating the DAC. If the sample had significant preferred orientation, the sound velocity should change with the angle. However, as shown in *SI Appendix, Fig. S6A*, the variation of the sound velocities of Fe-Brd with the rotation angle was within the experimental error of 1%. These values are small compared to that of MgO single crystal in the (100) crystallographic plane, which was within 4% at 14.6 GPa (63). This result strongly strengthens the robustness of our Brillouin data (25) (see also *SI Appendix, Supplementary Discussion*). We calculated experimental uncertainties of all data including propagated errors

of the acoustic velocities as a function of the rotational angle in the scattered plane.

Identification by Raman Spectroscopy. For preliminary phase identification, in situ high-pressure Raman spectroscopic measurement was carried out in a DAC to pressures of 105.8 GPa at room temperature. The 457.9-nm line of an argon ion laser (Innova 90, Coherent) with an output power near 150 mW was used for sample excitation in the Raman scattering measurements. The laser beam was focused to $\sim 10\text{ }\mu\text{m}$ on the sample. The acquisition time was 30 min. Raman spectrum taken at 105.1 GPa is shown in *SI Appendix, Fig. S6B*. Almost all of the peaks can be indexed as Fe-Brd.

TEM-EELS Analysis of $\text{Fe}^{3+}/\Sigma\text{Fe}$ Ratios. Recovered samples from our DAC experiments were sectioned using a Ga^+ focused ion beam (FIB) instrument at University of Bayreuth (FEI, Scios DualBeam). During FIB sectioning, the samples were monitored by scanning electron microscopy using back-scattered electrons to precisely locate the centers of the measured spots of Brillouin experiments. Sections were removed via an in situ micromanipulator, mounted on Cu grids using Pt deposition, and thinned to $\sim 80\text{-nm}$ thickness by the Ga^+ ion beam for analysis for EELS. These FIB lamellae were analyzed by analytical TEM in order to determine the $\text{Fe}^{3+}/\Sigma\text{Fe}$ ratios, and obtain the chemical composition and structural information. TEM analysis was performed using an FEI Titan G2 80–200 TEM/STEM (Scanning Transmission Electron) microscope and Philips CM20 FEG (field-emission gun) system at University of Bayreuth, equipped with an EDX analyzer and EELS, operated at 200 kV. The SAED patterns and EELS spectra were taken at $-170\text{ }^\circ\text{C}$ using a liquid-nitrogen-cooling holder. We show the typical bright-field TEM images of the recovered samples in Fig. 1 C and D. From Fig. 1 C and D we can clearly observe the fine grains of Fe-Brd ($<500\text{ nm}$) which are sufficiently smaller than the measured spots of Brillouin experiments ($\sim 10\text{ }\mu\text{m}$), apparently showing that the sample did not suffer significant grain growth or preferred orientation. Therefore, we can assume that the peaks obtained from the Brillouin spectra from a polycrystalline sample represent the average aggregate velocity. This result also strengthens the robustness of our Brillouin data (see also *SI Appendix, Supplementary Discussion*). The quantification of the EELS analyses (Fig. 1G) followed the procedure described by van Aken et al. (64, 65) using the available fitting program EELSA (<http://www.clemensprescher.com/programs/eelsa>). More technical details of the FIB milling and EELS method are described by Miyajima et al. (66). The determination of the $\text{Fe}^{3+}/\Sigma\text{Fe}$ ratio was based on intensity ratio of the $\text{Fe-L}_{2,3}$ white-line maxima. The spectrum has been gain-normalized, background-subtracted, and deconvoluted using the corresponding low-loss spectrum. The black dotted lines in Fig. 1G represent the position of the Fe-L_3 white-line maxima for Fe^{2+} (at $\sim 707.8\text{ eV}$, fixed for the energy calibration) and Fe^{3+} ($\sim 710\text{ eV}$), respectively. The time-series analyses showed that the measured ratios did not change remarkably with increasing irradiation time up to 40 s

Spatial Fe-Content Distributions of the Recovered Samples. *SI Appendix, Fig. S1 A and B* shows typical HAADF image of the recovered sample and the EDX element map of Fe. The Fe-rich spots within the Brd grains are (Mg, Fe)O Fp or metallic Fe. Those Fe-rich phases are undetectable as Brillouin peaks because of the small fraction (less than several percent). Spatial Fe-content distributions of the recovered samples are also given for the run#Brd01 and Brd02 in *SI Appendix, Fig. S1 C and D*. The measured areas of Fe contents correspond to the measured spots of Brillouin experiments. *SI Appendix, Fig. S1 C and D* shows the vertical (c) and horizontal (d) distributions to the culet surface of the DACs, respectively. The Fe contents of Brd given in this paper represents the mean value of the Brd regions in each run.

Data Availability. All study data are included in the article and *SI Appendix*.

ACKNOWLEDGMENTS. We appreciate S. Ozawa and K. Marquardt for their assistance with the experiments. We also appreciate D. J. Frost, E. Ohtani, T. Katsura, M. Nakamura, T. Kakegawa, T. Kimura, A. Suzuki, T. Kuribayashi, S. Okumura, and T. Ishii for their useful discussions. This work was supported by MEXT/JSPS (Ministry of Education, Culture, Sports, Science and Technology/Japan Society for the Promotion of Science) KAKENHI Grants 22684028, 24654170, and 25247087, and Start-up fund at ETH Zürich to M.M., and MEXT/JSPS KAKENHI Grants 15J02017 and 19K21049 to I.M. This work was also supported by the JSPS Japanese-German Graduate Externship. S.P. is financed through a DFG (Deutsche Forschungsgemeinschaft) project (PE 2334/1-1). The Scios FIB and the Titan G2 TEM at BGI (Bayerisches Geoinstitut) were financed by DFG Grants INST 91/315-1 FUGG and INST 91/251-1 FUGG, respectively.

1. W. F. McDonough, S. S. Sun, The composition of the Earth. *Chem. Geol.* **120**, 223–253 (1995).
2. C. J. Allègre, J. P. Poirier, E. Humler, A. W. Hofmann, The chemical composition of the Earth. *Earth Planet. Sci. Lett.* **134**, 515–526 (1995).
3. T. Lyubetskaya, J. Korenaga, Chemical composition of Earth's primitive mantle and its variance: 1. Method and results. *J. Geophys. Res. Solid Earth* **112**, B03211 (2007).
4. M. Murakami, J. D. Bass, Evidence of denser MgSiO₃ glass above 133 gigapascal (GPa) and implications for remnants of ultradense silicate melt from a deep magma ocean. *Proc. Natl. Acad. Sci. U.S.A.* **108**, 17286–17289 (2011).
5. M. Murakami, Y. Ohishi, N. Hirao, K. Hirose, A perovskitic lower mantle inferred from high-pressure, high-temperature sound velocity data. *Nature* **485**, 90–94 (2012).
6. J.-F. Lin *et al.*, Spin transition of iron in magnesiowüstite in the Earth's lower mantle. *Nature* **436**, 377–380 (2005).
7. J. F. Lin *et al.*, Spin transition zone in Earth's lower mantle. *Science* **317**, 1740–1743 (2007).
8. S. Speziale *et al.*, Effects of Fe spin transition on the elasticity of (Mg, Fe)O magnesiowüstites and implications for the seismological properties of the Earth's lower mantle. *J. Geophys. Res. Solid Earth* **112**, B10212 (2007).
9. J. F. Lin, T. Tsuchiya, Electronic spin transition of iron in the Earth's lower mantle. *Phys. Earth Planet. Inter.* **170**, 248–259 (2008).
10. D. Antonangeli *et al.*, Spin crossover in ferropericlasite at high pressure: A seismologically transparent transition? *Science* **331**, 64–67 (2011).
11. Z. Wu, R. M. Wentzcovitch, Spin crossover in ferropericlasite and velocity heterogeneities in the lower mantle. *Proc. Natl. Acad. Sci. U.S.A.* **111**, 10468–10472 (2014).
12. Z. Wu, R. M. Wentzcovitch, Composition versus temperature induced velocity heterogeneities in a pyrolytic lower mantle. *Earth Planet. Sci. Lett.* **457**, 359–365 (2017).
13. J. Badro *et al.*, Electronic transitions in perovskite: Possible nonconvecting layers in the lower mantle. *Science* **305**, 383–386 (2004).
14. C. McCammon *et al.*, Stable intermediate-spin ferrous iron in lower-mantle perovskite. *Nat. Geosci.* **1**, 684–687 (2008).
15. I. Kupenko *et al.*, Oxidation state of the lower mantle: In situ observations of the iron electronic configuration in bridgmanite at extreme conditions. *Earth Planet. Sci. Lett.* **423**, 78–86 (2015).
16. G. Shukla *et al.*, Thermoelasticity of Fe²⁺-bearing bridgmanite. *Geophys. Res. Lett.* **42**, 1741–1749 (2015).
17. H. Hsu, R. M. Wentzcovitch, First-principles study of intermediate-spin ferrous iron in the Earth's lower mantle. *Phys. Rev. B Condens. Matter Mater. Phys.* **90**, 195205-1–195205-10 (2014).
18. S. Fu *et al.*, Abnormal elasticity of Fe-bearing bridgmanite in the Earth's lower mantle. *Geophys. Res. Lett.* **45**, 4725–4732 (2018).
19. D. J. Frost *et al.*, Experimental evidence for the existence of iron-rich metal in the Earth's lower mantle. *Nature* **428**, 409–412 (2004).
20. C. A. McCammon, Perovskite as a possible sink for ferric iron in the lower mantle. *Nature* **387**, 694–696 (1997).
21. C. McCammon, Geochemistry. The paradox of mantle redox. *Science* **308**, 807–808 (2005).
22. A. Kurnosov, H. Marquardt, D. J. Frost, T. B. Ballaran, L. Ziberna, Evidence for a Fe³⁺-rich pyrolytic lower mantle from (Al,Fe)-bearing bridgmanite elasticity data. *Nature* **543**, 543–546 (2017).
23. J. F. Lin, Z. Mao, J. Yang, S. Fu, Elasticity of lower-mantle bridgmanite. *Nature* **564**, E18–E26 (2018).
24. J. Chantel, D. J. Frost, C. A. McCammon, Z. Jing, Y. Wang, Acoustic velocities of pure and iron-bearing magnesium silicate perovskite measured to 25 GPa and 1200 K. *Geophys. Res. Lett.* **39**, L19307 (2012).
25. I. Mashino, M. Murakami, E. Ohtani, Sound velocities of δ -AlOOH up to core-mantle boundary pressures with implications for the seismic anomalies in the deep mantle. *J. Geophys. Res. B Solid Earth* **121**, 595–609 (2016).
26. T. S. Duffy, D. L. Anderson, Seismic velocities in mantle minerals and the mineralogy of the upper mantle. *J. Geophys. Res.* **94**, 1895 (1989).
27. S. Lundin *et al.*, Effect of Fe on the equation of state of mantle silicate perovskite over 1 Mbar. *Phys. Earth Planet. Inter.* **168**, 97–102 (2008).
28. S. M. Dorfman, T. S. Duffy, Effect of Fe-enrichment on seismic properties of perovskite and post-perovskite in the deep lower mantle. *Geophys. J. Int.* **197**, 910–919 (2014).
29. M. Murakami, S. V. Sinogeikin, H. Hellwig, J. D. Bass, J. Li, Sound velocity of MgSiO₃ perovskite to Mbar pressure. *Earth Planet. Sci. Lett.* **256**, 47–54 (2007).
30. B. Kiefer, L. Stixrude, R. M. Wentzcovitch, Elasticity of (Mg, Fe)SiO₃-Perovskite at high pressures. *Geophys. Res. Lett.* **29**, 34-1–34-4 (2002).
31. R. Caracas, R. E. Cohen, Effect of chemistry on the stability and elasticity of the perovskite and post-perovskite phases in the MgSiO₃-FeSiO₃-Al₂O₃ system and implications for the lowermost mantle. *Geophys. Res. Lett.* **32**, 1–4 (2005).
32. I. Jackson, S. M. Rigden, "9 - Composition and Temperature of the Earth's Mantle: Seismological Models Interpreted through Experimental Studies of Earth Materials" in *The Earth's Mantle: Composition, Structure, and Evolution* (I. Jackson, Ed.), (Cambridge University Press, 1998), pp. 405–460.
33. G. Shukla, M. Cococcioni, R. M. Wentzcovitch, Thermoelasticity of Fe³⁺- and Al-bearing bridgmanite. *Geophys. Res. Lett.* **43**, 5661–5670 (2016).
34. L. Stixrude, C. Lithgow-Bertelloni, Thermodynamics of mantle minerals - I. Physical properties. *Geophys. J. Int.* **162**, 610–632 (2005).
35. E. Mattern, J. Matas, Y. Ricard, J. Bass, Lower mantle composition and temperature from mineral physics and thermodynamic modelling. *Geophys. J. Int.* **160**, 973–990 (2005).
36. S. Cottaar, T. Heister, I. Rose, C. Unterborn, BurnMan: A lower mantle mineral physics toolkit. *Geochem. Geophys. Geosyst.* **15**, 1164–1179 (2014).
37. T. Katsura, A. Yoneda, D. Yamazaki, T. Yoshino, E. Ito, Adiabatic temperature profile in the mantle. *Phys. Earth Planet. Inter.* **183**, 212–218 (2010).
38. O. L. Anderson, The Earth's core and the phase diagram of iron. *Philos. Trans. R. Soc. London A Math. Phys. Eng. Sci.* **306**, 21–35 (1982).
39. A. M. Dziewonski, D. L. Anderson, Preliminary reference Earth model. *Phys. Earth Planet. Inter.* **25**, 297–356 (1981).
40. J. Li *et al.*, Electronic spin state of iron in lower mantle perovskite. *Proc. Natl. Acad. Sci. U.S.A.* **101**, 14027–14030 (2004).
41. K. Catali *et al.*, Effects of the Fe³⁺ spin transition on the properties of aluminous perovskite-New insights for lower-mantle seismic heterogeneities. *Earth Planet. Sci. Lett.* **310**, 293–302 (2011).
42. I. Mashino *et al.*, Chemistry and mineralogy of Earth's mantle: the spin state of iron in Fe³⁺-bearing Mg-perovskite and its crystal chemistry at high pressure. *Am. Mineral.* **99**, (2014).
43. R. Sinmyo, C. McCammon, L. Dubrovinsky, The spin state of Fe³⁺ in lower mantle bridgmanite. *Am. Mineral.* **102**, 1263–1269 (2017).
44. I. Kupenko *et al.*, Electronic spin state of Fe,Al-containing MgSiO₃ perovskite at lower mantle conditions. *Lithos* **189**, 167–172 (2014).
45. T. Komabayashi, K. Hirose, Y. Nagaya, E. Sugimura, Y. Ohishi, High-temperature compression of ferropericlasite and the effect of temperature on iron spin transition. *Earth Planet. Sci. Lett.* **297**, 691–699 (2010).
46. Y. Fei *et al.*, Spin transition and equations of state of (Mg, Fe)O solid solutions. *Geophys. Res. Lett.* **34**, 1–5 (2007).
47. A. Ricolleau *et al.*, Density profile of pyrolite under the lower mantle conditions. *Geophys. Res. Lett.* **36**, 1–5 (2009).
48. E. Mattern, J. Matas, Y. Ricard, J. Bass, Lower mantle composition and temperature from mineral physics and thermodynamic modelling. *Geophys. J. Int.* **160**, 973–990 (2005).
49. J. Matas, J. Bass, Y. Ricard, E. Mattern, M. S. T. Bukowski, On the bulk composition of the lower mantle: Predictions and limitations from generalized inversion of radial seismic profiles. *Geophys. J. Int.* **170**, 1–42 (2005).
50. B. J. Wood, M. J. Walter, J. Wade, Accretion of the Earth and segregation of its core. *Nature* **441**, 825–833 (2006).
51. A. S. Wolf, J. M. Jackson, P. Dera, V. B. Prakapenka, The thermal equation of state of (Mg, Fe)SiO₃ bridgmanite (perovskite) and implications for lower mantle structures. *J. Geophys. Res. Solid Earth* **120**, 7460–7489 (2015).
52. X. Wang, T. Tsuchiya, A. Hase, Computational support for a pyrolytic lower mantle containing ferric iron. *Nat. Geosci.* **8**, 556–559 (2015).
53. G. R. Heffrich, B. J. Wood, The Earth's mantle. *Nature* **412**, 501–507 (2001).
54. J. H. Davies, J. P. Brodholt, B. J. Wood, Chemical reservoirs and convection in the Earth's mantle-Introduction. *Philos. Trans. R. Soc. Lond. A* **360**, 2361–2369 (2002).
55. Y. Fukao, S. Widiyantoro, M. Obayashi, Stagnant slabs in the upper and lower mantle transition region. *Rev. Geophys.* **39**, 291–323 (2001).
56. M. D. Ballmer, N. C. Schmerr, T. Nakagawa, J. Ritsema, Compositional mantle layering revealed by slab stagnation at ~1000-km depth. *Sci. Adv.* **1**, e1500815 (2015).
57. V. Steinbach, D. A. Yuen, Effects of depth-dependent properties on the thermal anomalies produced in flush instabilities from phase transitions. *Phys. Earth Planet. Inter.* **86**, 165–183 (1994).
58. U. R. Christensen, D. A. Yuen, Layered convection induced by phase transitions. *J. Geophys. Res.* **90**, 10291 (1985).
59. A. Gando *et al.*, Reactor on-off antineutrino measurement with KamLAND. *Phys. Rev. D Part. Fields Gravit. Cosmol.* **88**, 033001 (2013).
60. A. E. Ringwood, A model for the upper mantle. *J. Geophys. Res.* **67**, 857–867 (1962).
61. J. P. Poirier, *Introduction to the Physics of the Earth's Interior* (Cambridge University Press, 2000).
62. H. K. Mao, J. Xu, P. M. Bell, Calibration of the ruby pressure gauge to 800 kbar under quasi-hydrostatic conditions. *J. Geophys. Res.* **91**, 4673 (1986).
63. S. V. Sinogeikin, J. D. Bass, Single-crystal elasticity of pyrope and MgO to 20 GPa by Brillouin scattering in the diamond cell. *Phys. Earth Planet. Inter.* **120**, 43–62 (2000).
64. P. A. van Aken, B. Liebscher, V. J. Styrja, Quantitative determination of iron oxidation states in minerals using Fe L_{2,3}-edge electron energy-loss near-edge structure spectroscopy. *Phys. Chem. Miner.* **25**, 323–327 (1998).
65. P. A. van Aken, B. Liebscher, Quantification of ferrous/ferric ratios in minerals: New evaluation schemes of Fe L₂₃ electron energy-loss near-edge spectra. *Phys. Chem. Miner.* **29**, 188–200 (2002).
66. N. Miyajima *et al.*, Combining FIB milling and conventional Argon ion milling techniques to prepare high-quality site-specific TEM samples for quantitative EELS analysis of oxygen in molten iron. *J. Microsc.* **238**, 200–209 (2010).